coatings

MDPI

Article

Development of the Zn-ZnO(Nw)@$CuMnO_2$ Heterojunction by Low Temperature Zn Foil Oxidation for Gas Sensor Fabrication

Mircea Nicolaescu [1,2,†], Cornelia Bandas [1,†], Corina Orha [1,†], Violeta Purcar [3] and Carmen Lazau [1,*]

1 National Institute for Research and Development in Electrochemistry and Condensed Matter Timisoara, Dr. A.P. Podeanu No.144, 300569 Timisoara, Romania
2 Department of Materials and Manufacturing Engineering, Faculty of Mechanical Engineering, "Politehnica" University of Timisoara, P-ta Victoriei No.2, 300006 Timisoara, Romania
3 National Institute for Research & Development in Chemistry and Petrochemistry—ICECHIM, Splaiul Independentei 202, 6th District, 060021 Bucharest, Romania
* Correspondence: carmen.lazau@gmail.com
† Contributed equally to this work as first authors.

Abstract: In this study, the Zn-ZnO(Nw)@$CuMnO_2$ heterostructure was successfully achieved by deposition of a bidimensional $CuMnO_2$ film on the ZnO nanowires (NWs) layer, by the spin coating method. The novelty of this research is related to the growth of ZnO NWs by thermal oxidation at low temperatures, below the melting point of the Zn foil in a controlled atmosphere consisting of a mixed flow gas, Ar and O_2. The structural and morphological properties of the heterostructures were assessed by XRD, UV-Vis, and SEM techniques. The as-obtained gas sensors based on Zn-ZnO(Nw)@$CuMnO_2$ heterostructures were tested to detect 400 ppm. CO_2 concentration at variable testing temperatures inside the testing chamber. The maximum sensibility value of 85.5% was obtained at the lowest operating temperature of 150 °C for the ZnO_{Nw5}@CMO sensor, and when the temperature was increasing to 200 °C the sensibility response of 95.4% was recorded for the ZnO_{Nw7}@CMO sensor. Current-voltage and current-time measurements were performed under different conditions to assess the heterojunction behavior and sensibility of the gas sensor.

Keywords: semiconductors; electrical properties; "*n-p*" heterojunction; ZnO-$CuMnO_2$; sensor

Citation: Nicolaescu, M.; Bandas, C.; Orha, C.; Purcar, V.; Lazau, C. Development of the Zn-ZnO(Nw)@$CuMnO_2$ Heterojunction by Low Temperature Zn Foil Oxidation for Gas Sensor Fabrication. *Coatings* **2022**, *12*, 1630. https://doi.org/10.3390/coatings12111630

Academic Editor: Choongik Kim

Received: 30 September 2022
Accepted: 25 October 2022
Published: 27 October 2022

1. Introduction

Due to the progress of society and the development of technology, the considerable problems of air pollution have raised increasing problems in the environment and especially in human life. In recent decades, low-cost, small, sensitive, selective, and reliable gas sensors with reduced power consumption and enhanced performance have received a lot of attention because of their usefulness for detecting flammable or toxic gases. Today, several research efforts have been conducted to help develop and improve different types of gas sensors.

The increase in the concentration of CO_2 in the atmosphere is one of the main causes of climate change, leading to global warming. Furthermore, long-term exposure to high concentrations of CO_2 can be lethal to humans. Carbon dioxide (CO_2) sensors play an important role in various applications, such as air quality and greenhouse gas monitoring, fire detection, intelligent food packaging, medical diagnosis, and electronics [1,2]. Currently, many researchers have pursued the development of inexpensive and miniaturized CO_2 sensors, so there are many types of CO_2 gas sensors, such as gas chromatography (GC) and mass spectrometer (MS) [3], Severinghaus electrode [4], optical [5], electrochemical [6], acoustic [7], work function [8], and capacitive-based sensors [9,10]. Therefore, it is necessary to implement a sensor that can detect CO_2 in the air with excellent sensitivity and

with good response and recovery times. Metal oxides that are characterized as semiconducting transition (TiO_2, Fe_2O_3, NiO, Cr_2O_3) and post-transition (ZnO, SnO_2) are good candidates to be used as gas sensors. Moreover, these oxides are presented in different morphologies, sizes, and nanostructures (nanoparticles (NP), nanotubes (NT), nanocenters and nanowires (NWs)), they are found at low cost and flexible production, show high sensitivity and portability [11,12]. Due to their remarkable performance in electronics, optics, and photonics, ZnO nanoparticles are attractive candidates for many applications such as UV lasers, light-emitting diodes, solar cells, nanogenerators, gas sensors, photodetectors, and photocatalysts [13]. ZnO nanostructures with various morphologies, including wires [14], belts [15], tubes [16], rods [17], rings [18], sheets [19], and tetrapods [20] can be easily synthesized using chemical vapor deposition (CVD) [21], infrared irradiation, thermal evaporation, and thermal decomposition [22], laser-assisted vapor–liquid–solid growth [23], electrochemical deposition, sol-gel method and hydrothermal process [24,25]. The thermal oxidation technique can be used to fabricate ZnO nanowires because it is a relatively facile, low-cost, nonhazardous, and high-quality technique. In this case, temperature plays an important role in the thermal oxidation process, usually varying from 200 °C to 1000 °C [26]. Depending on the melting temperature (420 °C) and the boiling temperature (907 °C) of zinc, its oxidation mechanism can vary with the annealing temperature, so the morphology of the grown ZnO nanostructures can be changed from nanowires to tetrapods. This happens when the applied temperatures are below the zinc melting point or between the melting and boiling points of zinc or above the Zn boiling point, respectively. ZnO NWs are one of the most studied metal oxide nanostructures due to their wide potential applications in electronics, optoelectronics, sensors, energy harvesting devices, superhydrophobic surfaces, etc. [27,28]. The synergy between ZnO and other metal oxides forms a heterojunction that enhances gas-sensing properties. *B. Huang et al.* prepared n-ZnO@n-In_2O_3 core–shell nanofibers by electrospinning and demonstrated that since the Fermi level of In_2O_3 is higher than that of ZnO, electrons will be transferred from In_2O_3 to ZnO until the Fermi level of the two materials reaches equilibrium, and thus the depleted electron layer is formed on the In_2O_3 side. The formation of the depleted electron layer affects the barrier and electron transport of the material, thereby improving the gas sensitivity. The test results also indicated that the response of 57.98 of the ZnO@In_2O_3 core–shell nanofibers to 200 ppm ethanol at 225 °C was reached [29]. *C.-J. Chang et al.* successfully synthesized some structures based on ZnO nanorods [30] and Ce-doped ZnO nanorods, respectively, for fabrication of NO_2 gas sensors at low temperature of 100 °C [31]. *C. Han et al.* combined electrospinning, atomic layer deposition technology, and calcination to controllably prepare one-dimensional hollow p-CuO/n-ZnO nanofibers and analyzed the gas sensing properties of H_2S. The results showed that the construction of the CuO/ZnO heterostructure was approximately 6 and 45 times higher than that of pure ZnO and pure CuO [32–34]. *C. L. Hsu et al.* have synthesized nanostructured *n*-ZnO/*p*-$CuMnO_2$ core–shell nanowires by the sol-gel method that can improve the gas detection and photoresponse of these nanomaterials [35].

$CuMnO_2$ is a p-type of metal oxides known as the delafossite type and in combination with n-type oxides (e.g., TiO_2, ZnO), the resulting heterojunctions have high sensing properties for application in sensor devices [36]. *M. Nicolaescu et al.* obtained good results in the field of light detection by synthesizing UV photodetectors based on *n*-type TiO_2 and *p*-type $CuMnO_2$ heterojunction through a simple and low-cost method [37]. Furthermore, *C. Lazau et al.* reported the fabrication of a self-powered photodetector with the FTO/*n*-TiO_2/*p*-$CuMnO_2$ configuration, which demonstrated that the transparent heterojunction device of *n*-TiO_2/*p*-$CuMnO_2$ exhibited excellent properties in the self-powered mode with high sensitivity [38]. Taking into account the previous research results [36–38], within this paper, the research results are related to the growth of ZnO NWs by thermal oxidation at low temperature, to achieve the heterostructure type on Zn-ZnO(Nw)@$CuMnO_2$ with application as gas sensors for CO_2 detection.

2. Materials and Methods

2.1. Chemicals

All reagents were of analytical purity grade and used without further purification, as follows: Zn foil (thickness 0.25 mm, 99.9% purity), α-terpinol, ethyl cellulose, acetone, ethyl alcohol, $Cu(NO_3)_2 \cdot 3H_2O$, $Mn(NO_3)_2 \cdot 4H_2O$, sodium hydroxide were purchased from Sigma-Aldrich Company (*St. Louis, MO, USA*). The $CuMnO_2$ nanocrystalline compound used in this research was obtained by microwave-assisted hydrothermal method at 180 °C for 5 min using $Cu(NO_3)_2 \cdot 3H_2O$, $Mn(NO_3)_2 \cdot 4H_2O$ and sodium hydroxide, as previously reported [39].

2.2. Fabrication of Zn-ZnO(Nw)@$CuMnO_2$ Heterostructures

The achievement process of the Zn-ZnO(Nw)@$CuMnO_2$ heterostructures for the fabrication of the gas sensor is schematically illustrated in Figure 1. Initially, the Zn foil (an effective area of 1 × 1 cm) was cleaned with acetone, ethanol, and DI water in an ultrasonic bath, followed by drying at room temperature and treated for 30 min in UV ozone Cleaner (*Ossila Producer*). For the formation of Zn-ZnO (NW) structures, the thermal oxidation of Zn foil was performed in a tubular furnace in a controlled atmosphere of mixed gas flow Ar and O_2, with a controlled flow of 100 mL/min. The working parameters (temperature and time) and sample codes are presented in Table 1. The as-obtained Zn-ZnO (NW) structures were used for sensor fabrication, except for the support obtained at 300 °C for 6 h (Zn-ZnO_{Nw1}), as it was observed that the ZnO layer grew insufficiently for the studies proposed in this work. The deposition of the $CuMnO_2$ film (0.1 g of $CuMnO_2$ solution diluted with 1 mL ethanol) on the Zn-ZnO (NW) structures was achieved by the spin-coating method (*WS-400-6NPPB Spin Coater-Laurell Technology Corporation*), with a speed rotation of 2000 rpm for 10 s, the process being repeated twice. The deposition solution based on the 0.3 g $CuMnO_2$ powder, ethylcellulose (6 mL) and α-terpinol (6 mL) was mixed in the ball mill (*Lab Mills lx QM vertical planetary ball mill*) at a frequency of 40 kHz for 15 h. Finally, a thermal treatment at 250 °C for 1 h was applied to the as-obtained Zn-ZnO(Nw)@$CuMnO_2$ heterostructures. To collect measurement parameters, metal wires were affixed with silver paste, as follows, one wire on the Zn foil (in contact with ZnO "*n*" component) and the other on the $CuMnO_2$ film ("*p*" component).

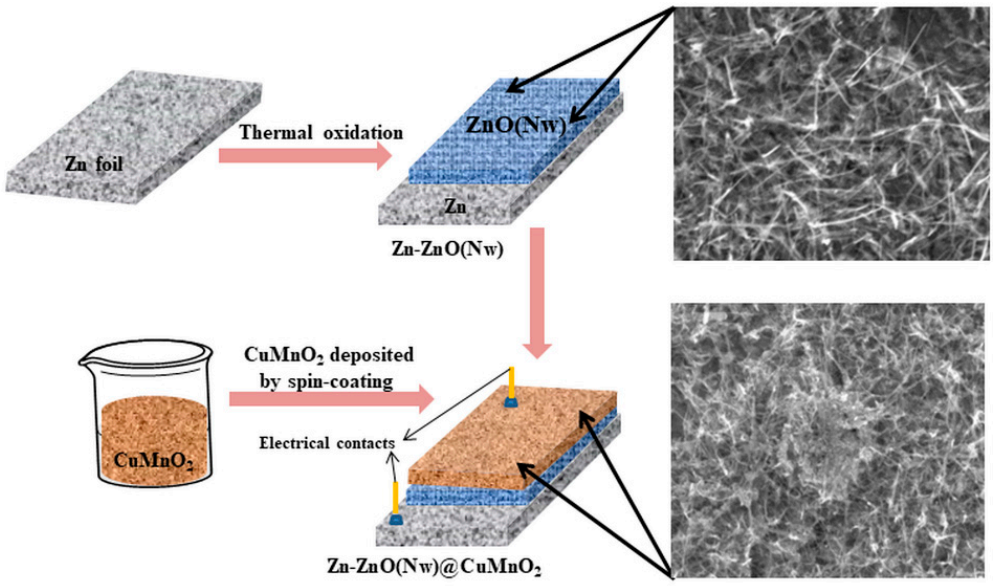

Figure 1. Schematic illustration of the gas sensor achievement process.

Table 1. The working parameters for the thermal oxidation of the Zn foil, ZnO crystallite sizes, the average length of ZnO NWsand sensor code.

Sample Support	ZnO Crystallite Size (nm)	ZnO (NWs) Length (nm)	Temperature (°C)	Time (h)	Sensor Code
Zn-ZnO$_{Nw1}$	15.40	-	300	6	*ZnO$_{Nw1}$@CMO*
Zn-ZnO$_{Nw2}$	15.40	54.49	350	2	*ZnO$_{Nw2}$@CMO*
Zn-ZnO$_{Nw3}$	16.20	46.18		4	*ZnO$_{Nw3}$@CMO*
Zn-ZnO$_{Nw4}$	17.70	62.17		6	*ZnO$_{Nw4}$@CMO*
Zn-ZnO$_{Nw5}$	22.06	91.03	400	2	*ZnO$_{Nw5}$@CMO*
Zn-ZnO$_{Nw6}$	23.28	134.33		4	*ZnO$_{Nw6}$@CMO*
Zn-ZnO$_{Nw7}$	22.34	85.29		6	*ZnO$_{Nw7}$@CMO*

2.3. Sensor Testing

To measure the response of the sensors, experiments were carried out in which the CO_2 gas concentration of 400 ppm was kept constant, and the working temperatures varied as follows: 25, 50, 100, 150, and 200 °C. All tests were performed in continuous gas flow with an applied voltage to the sensors of about 2 V and a humidity in the test chamber of about 50%. For assessment of response performance, the sensors were placed in a testing chamber equipped with humidity and temperature controllers. Thus, the heater (equipped with a temperature controller) was placed below the as-obtained sensor (*ZnO$_{NW}$@CMO*). To increase the flow turbulence and maximize the mixing of the gases, a mixer was placed prior to testing chamber. All components of the sensor testing installation are presented in Figure 2.

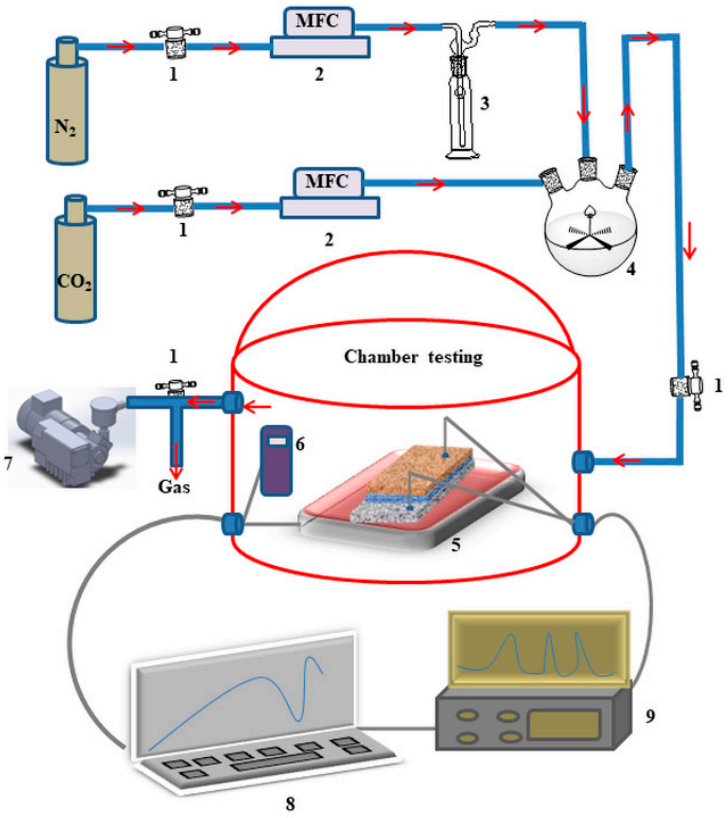

Figure 2. Schematic diagram of sensors testing: (1) valves; (2) mass flowmeter; (3) humidifier; (4) gas mixing chamber; (5) heater and temperature controller; (6) humidity sensor; (7) vacuum pump; (8) PC—data acquisition and processing; (9) Keithley 2450 SourceMeter.

The sensor testing experiment consisted of the following steps: *(a)* the sensor was placed and connected to the measuring devices in the test room; *(b)* vacuum was created in the installation; *(c)* argon was introduced, in flow, to clean the installation and the surface of the sensor; (*d)* vacuum was created in the installation; *(e)* the humidified CO_2-N_2 mixture was introduced and when the equilibrium state was reached. Before the next sensor testing experiment, the installation was extensively purged with nitrogen, and all previously presented steps were followed again.

2.4. Morpho-Structural, Electrical and Optical Characterization

X-ray diffraction analysis (*XRD, PANalytical X'Pert PRO MPD Diffractometer, Almelo, The Netherlands*) with Cu-Kα radiation (λ = 1.5418 Å) in the range of *2theta* = 20–80° was used for the structural characterization of the samples. The morphological properties of the as-obtained structures were studied by scanning electron microscopy (*SEM, FEI Inspect S model, Eindhoven, The Netherlands*) both for Zn-ZnO (NW) structures and for ZnO_{Nw}**@*CMO*** sensors. Electrical measurements of the as-obtained gas sensors were performed using the Keithley 2450 SourceMeter SMU Instrument (*Keithley Company, Cleveland, OH, USA*). Current-voltage (*I–V*) measurements were achieved for Zn-ZnO(Nw)@$CuMnO_2$ heterostructures in forward bias with '−' in the 'n' area (Zn electrode), and '+' in the metallic wire placed on the p-type semiconductor layer ($CuMnO_2$), applied voltage range between −2 V and + 2 V, with a step rate of 10 mV/s. To determine the band gap E_g by plotting Kubelka-Munk function against energy (*eV*), the optical analysis was recorded by UV-VIS analysis (*PerkinElmer Lambda 950 UV/Vis spectrophotometer, Shelton, CT, USA*).

3. Results and Discussion

3.1. Structural and Morphological Characteristics

Figure 3 shows the X-ray patterns for the as-synthesized heterostructures. In Figure 3a,b are presented the XRD spectra for Zn-ZnO (NW) structures obtained under different synthesis conditions, as presented in the experimental program described in Table 1. Thus, all peaks observed for the different Zn-ZnO (NW) supports presented at *2theta*: 31.6°, 34.4°, 36.2° and 47.5° (JCPDS 01-079-0205), respectively, confirmed the hexagonal structure of the ZnO crystal. Additionally, specific peaks of Zn from substrate foil were identified at *2theta:* 36.2°, 38.9° and 43.2° (JCPDS 00-001-1238). As can be seen, in all XRD patterns, a partial transformation from Zn to ZnO (NW) occurred due to the low working temperatures below the melting point of Zn (419 °C) [40]. With increasing oxidation temperature, ZnO peaks are more pronounced, and according to literature data the total transformation of Zn to ZnO is achieved at a temperature of 550 °C [41]. Additionally, the average crystallite sizes of the ZnO NWs presented in Table 1 were calculated using the Debye–Scherrer formula.

The XRD patterns of the as-synthesized sensors based on Zn-ZnO(Nw)@$CuMnO_2$ heterostructures presented in Figure 3c,d show that the specific peaks for $CuMnO_2$ (crednerite phase) at *2theta* are identified: 33.0°, 35.30°, 39.36°, 79.36° (JCPDS 01-071-1143) and Zn, ZnO, respectively, which proves the deposition of the $CuMnO_2$ films on the Zn-ZnO (NW) layers.

Figure 4 shows the SEM morphologies of the Zn-ZnO (NW) layers obtained at different temperatures and times, according to the experimental program shown in Table 1. Moreover, the average length of ZnO NWs was measured from SEM images using *imageJ* software, presented Table 1. From the SEM image, it can be seen that at an oxidation temperature of 300 °C for 6 h, there is an easy transition from nanoparticles to ZnO NWs on the surface of the Zn foil. By increasing the oxidation temperature to 350 °C, the ZnO NWs almost completely cover the surface of the Zn foil, and at the time of 6 h, the nanowires are well defined. At an oxidation temperature of 400 °C, the surface of the Zn foil is covered with a dense layer of ZnO and the growth directions of the nanowires are randomly oriented. Therefore, the length of ZnO NWs is directly proportional to the treatment time at an oxidation temperature of 400 °C.

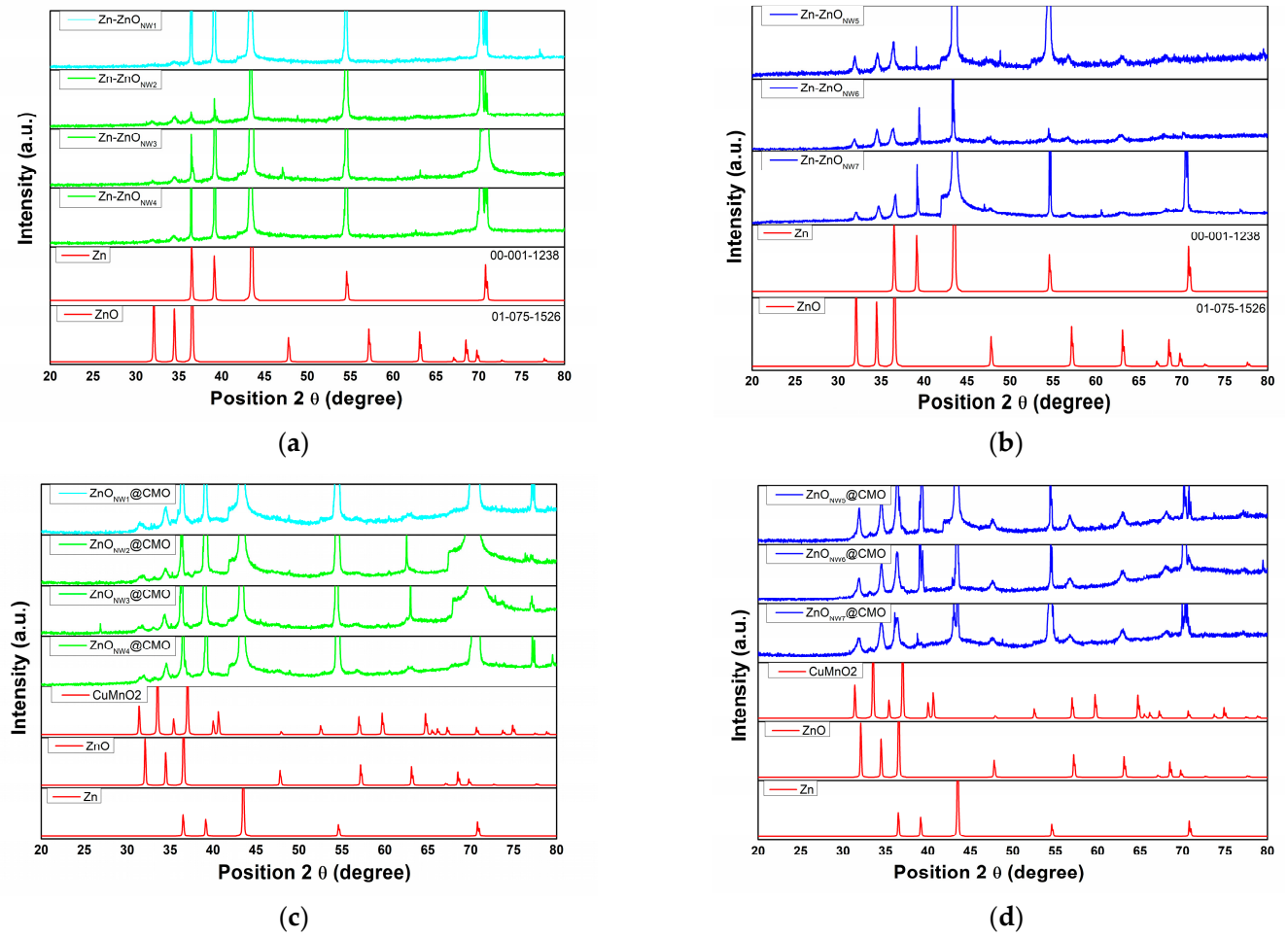

Figure 3. X-ray patterns for Zn-ZnO_{Nw} layers (**a**,**b**) and as-obtained ZnO_{Nw}***@CMO*** sensors (**c**,**d**).

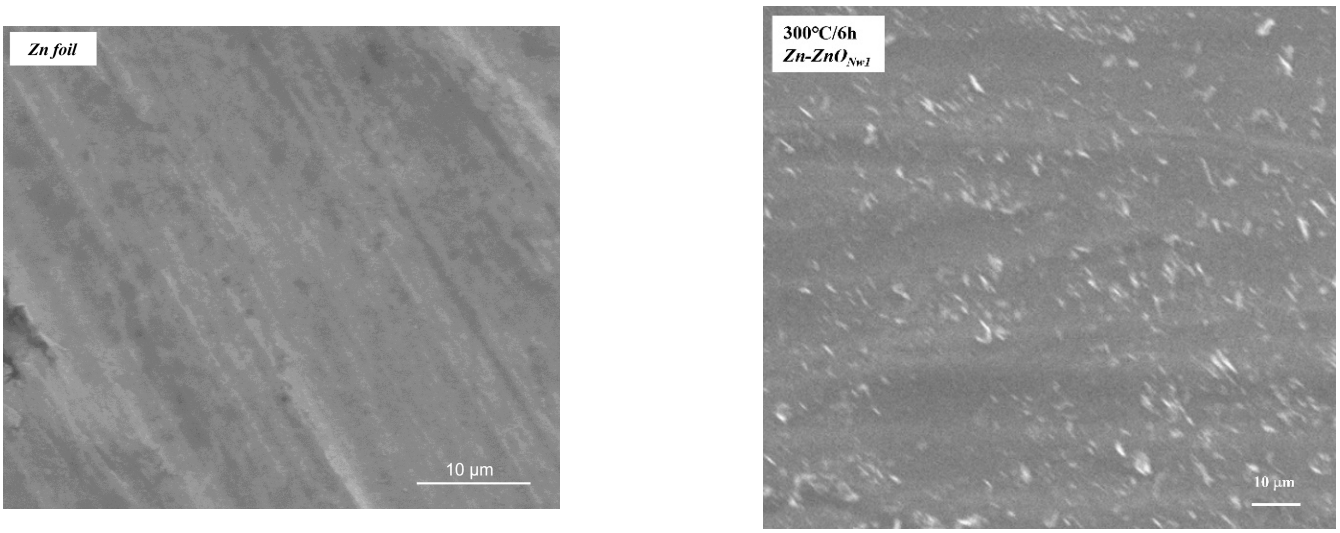

Figure 4. *Cont.*

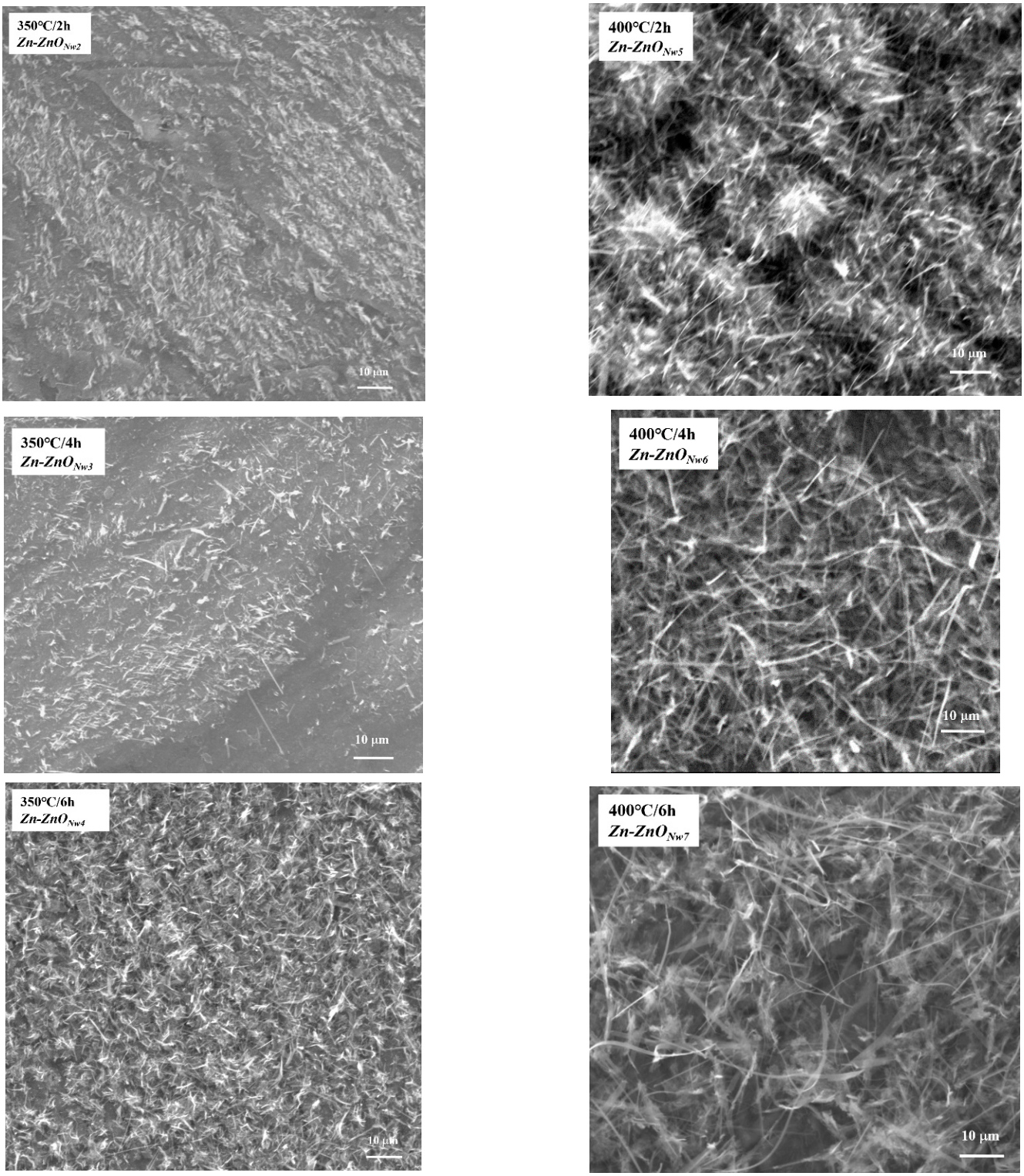

Figure 4. SEM morphologies of the Zn foil and Zn-ZnO_{Nw} layers.

The morphologies of the as-obtained ZnO_{Nw}**@*CMO*** sensors are presented in Figure 5. From the images, it can be observed that $CuMnO_2$ films completely coated the Zn-ZnO (NW) layers in the case of the ZnO_{Nw2}**@*CMO*,** ZnO_{Nw3}**@*CMO*** and ZnO_{Nw4}**@*CMO*** sensors, instead of the ZnO_{Nw5}**@*CMO*,** ZnO_{Nw6}**@*CMO*** and ZnO_{Nw7}**@*CMO*** sensors the $CuMnO_2$ film presents a nonuniform coating on the ZnO NWs, because of random growing of the ZnO NWs on the Zn foil surface.

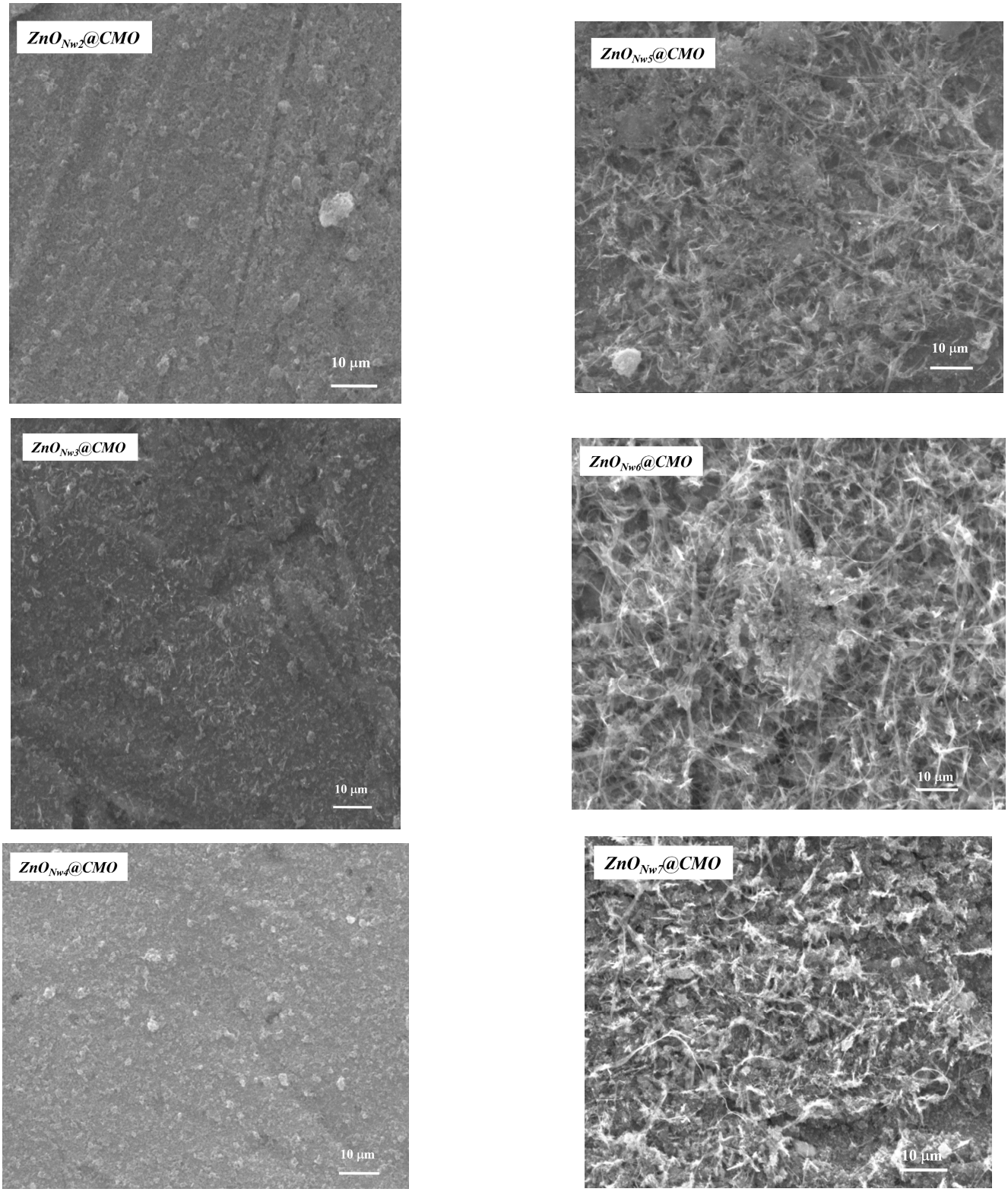

Figure 5. SEM morphology of the as-obtained ZnO_{Nw}**@CMO** sensors.

3.2. Optical and Electrical Properties

Figure 6 shows the optical band gap energy of the as-synthesized Zn-ZnO (NW) structures calculated by the *Tauc* plot using Equations (1) and (2), where α, hv, A and n denote the absorption coefficient, photon energy, a constant and an exponent, respectively.

The *Eg* optical band gap energy is derived from the intersection of the straight line with the *hv-axis* of the *Tauc* plot [37] (Figure 6a,b).

$$Eg = 1240/\gamma \quad (1)$$

$$\alpha h\nu = A(h\nu - Eg)^{n} \quad (2)$$

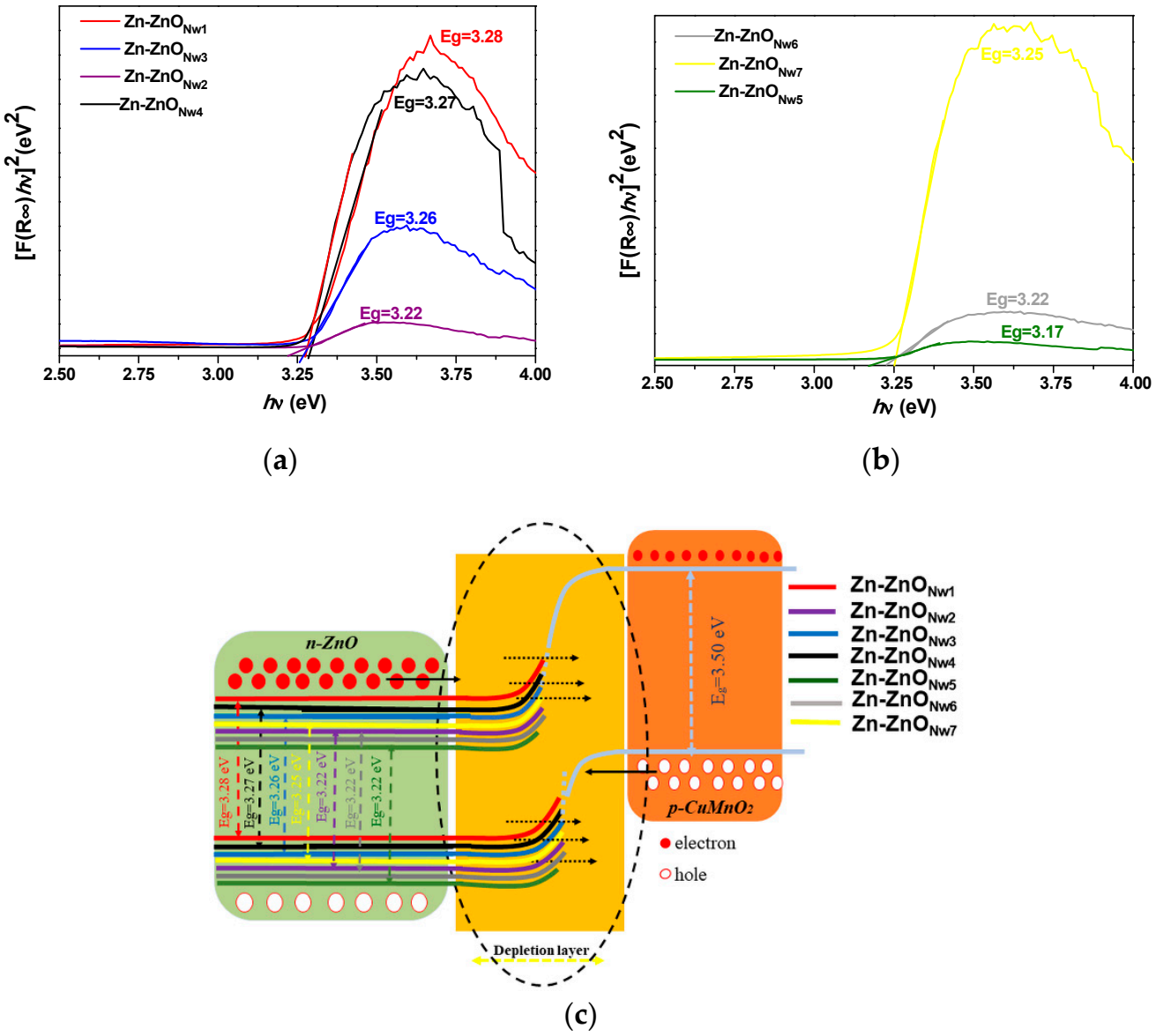

Figure 6. Band gap calculation *Eg* against energy (*eV*) for Zn-ZnO (NW) supports (**a**,**b**); Diagram for corresponding conduction and valence band edges (**c**).

The minimum and maximum band gaps of ZnO (NWs) are between 3.17 and 3.28 eV, for the samples synthesized at 300 °C and 400 °C. The band gap is slightly lower than the band gap energy at 3.37 eV of a perfect ZnO crystal [25]. Moreover, the thermal energy produced by heating the sample leads to a slight increase in the energy bandgap [42]. The *p*-type $CuMnO_2$ semiconductor has a slightly wide band gap at 3.5 eV [39]. The energy diagram of ZnO(NW)@$CuMnO_2$ heterojunction is presented in Figure 6c. Heterojunction metal oxide sensors compared with a single metal oxide sensor show improved performance in sensing targeted gases. When a different semiconductor is in contact, because of the different Fermi levels of the metal oxide in the as-constructed junctions lead to the

formation at the interface of a depletion layer and an accumulation layer. Because of the inconsistent Fermi levels of the metal oxide, the electrons will be transferred from the higher to lower Fermi levels until the junction reaches an equilibrium state, resulting in the formation of a potential barrier between them. The inflexion of the accumulation layer thickness influences the conductivity of the sensors; therefore, improving the gas sensitivity. Furthermore, the metal oxide heterojunction shows a higher specific surface area compared to single metal oxides. The higher specific surface area allows gas molecules to diffuse more lightly to the surface and have a higher probability of interaction with the junction, and it also ensures a more active surface [43].

Figure 7a–f presents the *I–V* curves of the experimental sensor type on ZnO_{Nw}@$CuMnO_2$ heterojunction, revealing a good rectifying behavior and demonstrating that the working parameters for the fabrication of the supports directly influence the electrical parameters. Thus, an increase in the forward bias current can be seen from 0.0082 mA for the ZnO_{Nw2}**@CMO** to 0.12 mA for the ZnO_{Nw4}**@CMO** sample, this increasing more than 100 times is due to the large number of charger carriers generated by the growth of ZnO on the Zn surface (Figure 7a–c). Instead, a decrease in current was observed for ZnO_{Nw5}**@CMO** from 0.043 mA to 0.0095 mA, probably generated by the narrowed heterojunction interface (Figure 7d). The *I-V* results show that the turn-on voltages vary nonlinear according to the holding time of the thermal oxidation process of the Zn foil, with a slight increase for the samples oxidized at 400 °C, this aspect can be associated with the increase in the specific surface area generated from the process parameters (Figure 7e,f). The high surface area to volume ratio of the ZnO_{NWs}@$CuMnO_2$ heterojunction enhances surface absorption, increasing charge carrier concentration in the depletion region. The rectifying behavior and an increase in the asymmetry between the forward and reverse bias are due to the *n*-ZnO/*p*-$CuMnO_2$ heterojunction, as ohmic contacts have been established between the electrodes and the semiconductor [44,45].

The thermionic emission relation was used to evaluate the current-voltage relationship of the characteristics of the established junction. The reverse saturation current (I_0) and the ideality factor (n) can be calculated as in our previous paper [38] from the line region of forward bias in the *Log (I)–V* plot, presented in the inset of Figure 7. The reverse saturation current (I_0) and the ideality factor (n), along with previous electrical parameters such as: turn-on voltage (V_T), current under forward bias (I_F), current under reverse bias (I_R) for all as-obtained sensors, are presented in Table 2.

Table 2. Electrical parameters of the as-obtained ZnO_{Nws}***@CMO*** sensor.

Sensors	V_T (V)	I_F (mA)	I_R (mA)	n	I_0 (A)
ZnO_{NW2}***@CMO***	0.801	8.2×10^{-4}	8.9×10^{-5}	4.17	8.41×10^{-7}
ZnO_{Nw3}***@CMO***	0.290	6.7×10^{-2}	5.6×10^{-2}	23.03	130×10^{-7}
ZnO_{Nw4}***@CMO***	0.780	12×10^{-2}	6.0×10^{-2}	27.81	134×10^{-7}
ZnO_{Nw5}***@CMO***	0.856	4.3×10^{-2}	1.5×10^{-2}	11.45	0.52×10^{-7}
ZnO_{Nw6}***@CMO***	0.359	6.6×10^{-3}	3.1×10^{-3}	21.16	3.72×10^{-7}
ZnO_{Nw7}***@CMO***	0.896	9.5×10^{-4}	3.5×10^{-4}	32.71	11.69×10^{-7}

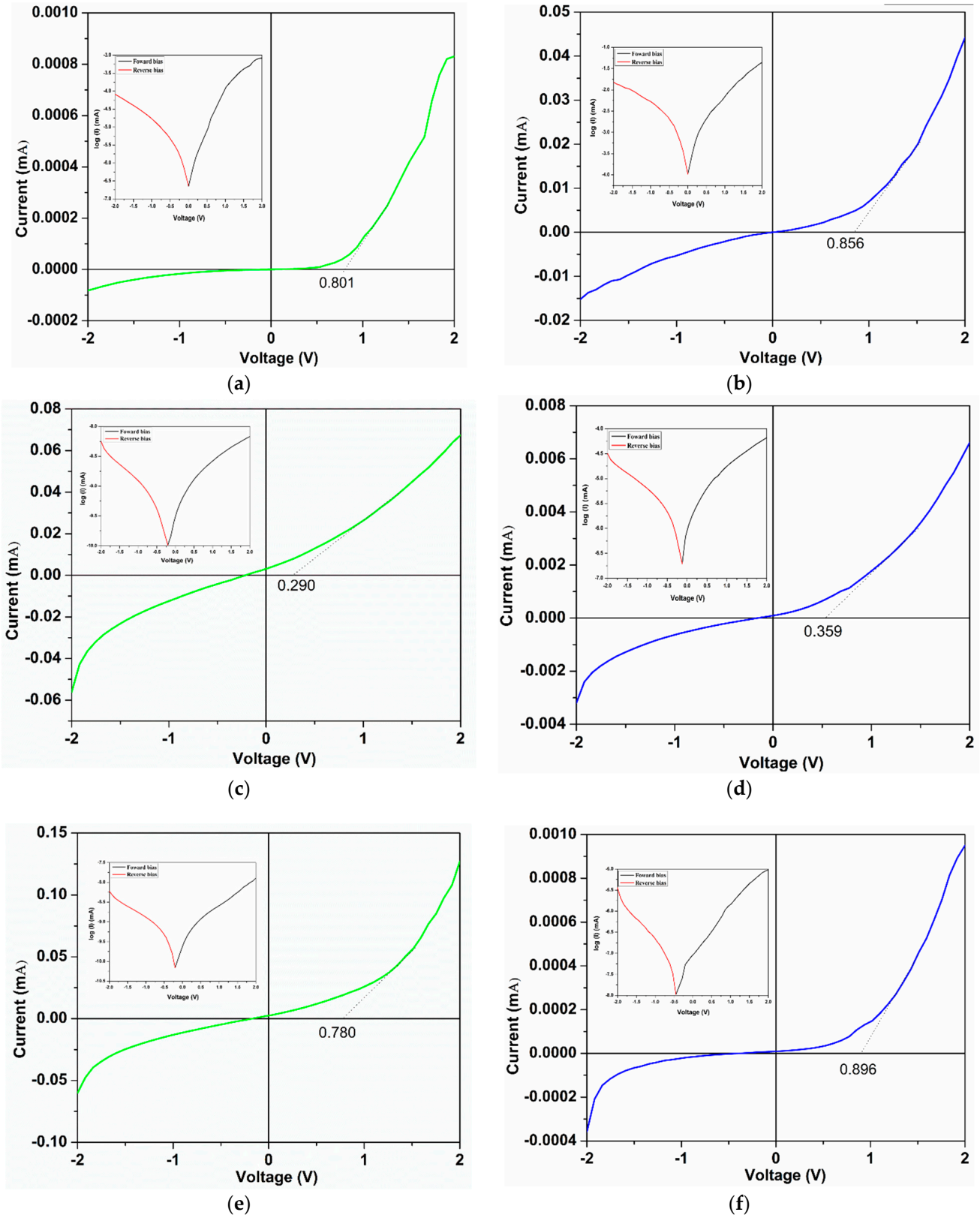

Figure 7. Current-voltage characteristics of the as-obtained sensors ZnO_{Nw2}**@CMO** (**a**); ZnO_{Nw3}**@CMO** (**b**); ZnO_{Nw4}**@CMO** (**c**); ZnO_{Nw5}**@CMO** (**d**); ZnO_{Nw6}**@CMO** (**e**); ZnO_{Nw7}**@CMO** (**f**) and Inset: *Log (I)–V* plot from forward and reverse bias.

The results show that for the as-obtained ZnO_{Nw3}**@*CMO***, ZnO_{Nw4}**@*CMO***, ZnO_{Nw6}**@*CMO***, and ZnO_{Nw7}**@*CMO*** sensors, the large ideality factor ($1 < n < 2$) indicates that the junction is far from ideal [46,47]. In the case of ZnO NWs, the zinc and oxygen layers parallel to the basal plane produce a dipole moment that leads to a potential gradient that influences the symmetry of the current flow along the c-axis [47,48]. However, in this study because the dipole orientation does not vary statistically between the wires, another explanation could be that different barrier heights are formed on both ends of the nanorod [49,50]. *Breitenstein et al.* introduced a mechanism to describe ideality factors, which is based on defects of the quasi-neutral zone and pair recombination from the junction [51]. Based on our results, the ideality factors increase proportionally with the working parameters for the Zn-ZnO_{Nws} supports sensor, confirming *Breitenstein et al.'s* model because with zinc oxidation, a greater number of defects appear [50,51]. Thus, the lower factor *n* at 4.17 for the heterojunction n-ZnO/p-$CuMnO_2$ is obtained for the ZnO_{Nw2}**@CMO** sensor (Zn foil at 350 °C/2 h) and the largest at 32.71 for the ZnO_{Nw7}**@CMO** sensor (Zn foil at 400 °C/6 h). The reverse saturation current is also directly proportional to the holding time and decreases at a higher oxidation temperature. This change in the reverse saturation current is the attribute of diffusion of minority charger carriers from the neutral region to the depletion region, generating a narrowed or increased heterojunction interface. Furthermore, from the semilogarithmic forward and reverse biases for the as-obtained ZnO_{Nws}**@*CMO*** sensors, a high increase in asymmetry between the forward and reverse biases is observed, showing that all heterojunctions work at a higher rectification value.

3.3. Sensing Properties of the ZnO_{Nw}@CMO Sensors

The sensing characteristics of the as-obtained ZnO_{Nws}**@CMO** sensors at 400 ppm CO_2 concentration and variable testing temperatures are presented in Figure 8. Response (*R*) was calculated based on Equation (3) [52], where I_{CO2} and I_{N2} indicate the current generated during the flow of CO_2 and N_2, respectively.

$$R = (I_{CO2} - I_{N2})/I_{N2} \times 100 \quad (3)$$

Figure 8a presents a plot of the testing temperature versus the response of the as-obtained sensors where the ZnO NWs were grown at 350 °C, demonstrating that a very low reaction occurred at a temperature below 100 °C. The response increased rapidly depending on the test sensor with increasing testing temperature, the maximum response value being obtained at 200 °C for all test sensors. The ZnO_{Nw4}**@CMO** sensor shows a high response at low temperature below 150 °C, but the maximum response is reached by the ZnO_{Nw3}**@CMO** sensor at a response value of approximately 77.5%, showing a dependence between the working parameters and the testing temperature in the testing chamber. Figure 8b presents the results of the testing temperatures versus the response of the ZnO NWs heterojunction sensor grown at 400 °C. A reduced response occurs at a temperature below 100 °C, where all tested sensors have approx. 17% response values. For the ZnO_{Nw5}**@CMO** sensor, the maximum value is at 150 °C and after that the response value declined. Instead, for the ZnO_{Nw6}**@CMO** and ZnO_{Nw7}**@CMO** sensors, the maximum values of the responses are at 200 °C, and these values linearly increase directly proportional to the testing temperature. The maximum response is obtained for the ZnO_{Nw7}**@CMO** sensor at 95.4%, indicating that a high surface area to volume ratio of ZnO_{NW} improves the response values. Table 3 summarize different morphologies and operating temperatures for CO and CO_2 detection.

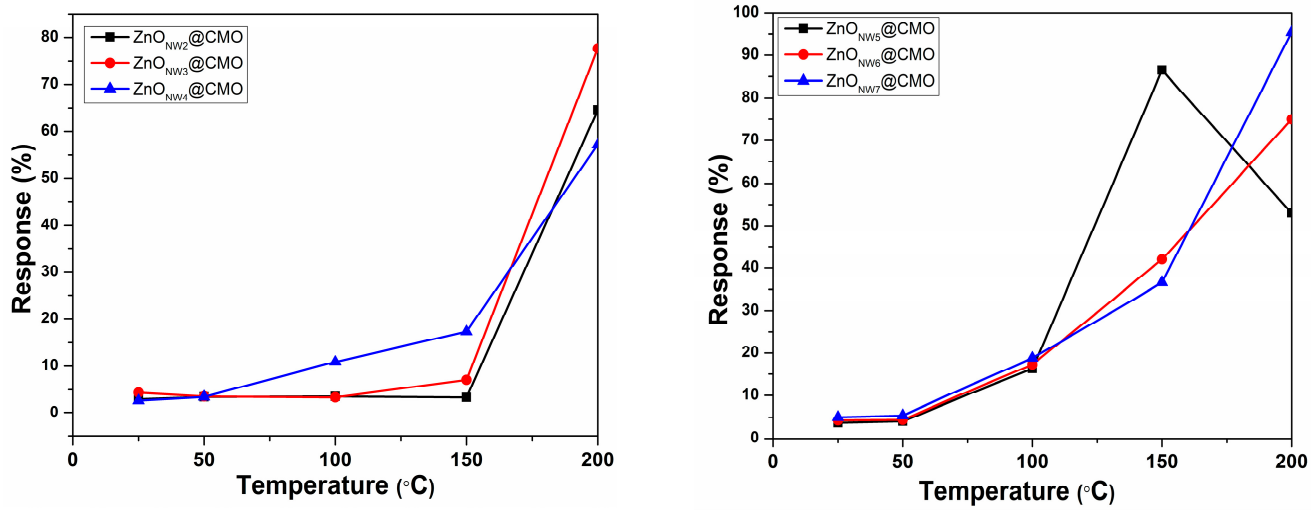

Figure 8. Diagram of the testing temperature and response of ZnO_{Nws}**@CMO** sensors at Zn foil oxidation temperature of 350 °C (**a**) and 400 °C (**b**).

Table 3. Different structures for CO and CO_2 detection.

Material	Morphologies	CO_2 (ppm)	Operating Temperature (°C)	Response (%)	Reference
Ti/TiO_2/LSCNO	Nanotubes	400	200	38.41	[52]
rGO/NiO-In_2O_3	Nanospheres	50	25	40	[53]
Au-ZnO	Nanowires	200	250	80	[54]
La-ZnO	Nanorods	5000	400	65	[55]
SnO2/CuO	nanofilm	500	180	12	[56]
Zn/ZnO/$CuMnO_2$	Nanowires	400	150	85.5	This work
Zn/ZnO/$CuMnO_2$	Nanowires	400	200	95.4	This work

A low crystallite size of ZnO NWs between 15 and 23 nm was obtaining by thermal oxidation of zinc plate (presented in Table 1). According to *Hung et al.*, an exponentially enhanced of the sensitivity is obtained when the grain size and the space-charge length are in the same range. Thus, for SnO_2 sensor the range of grain size/space-charge length was about 6 nm, this ratio allowing the sensors to be operated in the grain-controlled mode [57]. Moreover, *Chen et al.* presented a significantly improved in the gas sensitivity by decreasing the grain size (about 15 nm) of the ZnO NWs [58]. In our study, since a low increase in crystallite size is generated by the oxidation parameter, we do not find a direct relation of the crystallite size to sensor response. Thus, for the as-synthesized sensors we believe that the high response of the CO_2 sensor can be attributed to the small crystallite size and high surface-to-volume ratios associated with the poly-crystalline nanowires. Additionally, the surface-to-volume ratios of NWs generate by increasing the oxidation temperature is the principal parameter which improve the response in our case. For the as-described sensors, it is believed that the high sensitivity and reversibility under ambient conditions can be attributed to the intrinsically small crystallite size and high surface-to-volume ratios associated with the polycrystalline nanowires.

Because the working mechanism of the junction is not like a classical p-n junction, and the junction works more based on defects in the quasineutral zone and pair recombination from the interface, the junction parameter does not directly influence the response of the gas sensor. The heterojunction sensor in this study worked on the conductance of the film, and by the difference potential barrier of the n-p metal oxide. The oxidant gas is adsorbed

on the $CuMnO_2$ surface and introduces a potential barrier. Thus, a high-conductivity zone is formed that facilitates the mechanics of transport to the junction interface and generates an enlargement of the heterojunction interface, resulting in a good response device.

4. Conclusions

This work reports, for the first time, the growth of ZnO NWs by thermal oxidation in a mixed gas flow of 95% Ar and 5% O_2 at low temperature (300 °C and 400 °C) below the melting point of the Zn. Moreover, as-obtained sensors (ZnONw**@CMO** based on n-ZnO and p-$CuMnO_2$) with high detection response of CO_2 were successfully produced. The structural, morphological, optical, and electrical properties of the Zn-ZnO_{Nw} and ZnO_{Nw}**@CMO** structures were studied. From X-ray patterns, the hexagonal structure of the ZnO crystal and the specific peaks for $CuMnO_2$ (crednerite phase) were identified. The SEM morphology highlights that the transition from ZnO nanoparticles to ZnO NWs on the surface of the Zn foil is done gradually, depending on the treatment time and oxidation temperatures. Additionally, it was observed that the $CuMnO_2$ film was differently coated on the Zn-ZnO (NW) structures due to the density and random growth of the ZnO NWs on the Zn foil surface. From the optical measurements of ZnO NWs, a slightly higher band gap value at 3.28 eV is obtained for the sample synthesized at low temperature, probably because of the thermal energy of the treated sample. From the *I–V* measurement of heterojunctions, it was found that there is a directed correlation between the ideality factors and reverse saturation current and of the thermal oxidation process parameters of the Zn foil. The sensors tested in the experimental installation highlighted that at a CO_2 concentration of 400 ppm, the maximum response was 95.4%, obtained at a testing temperature of 200 °C for the ZnO_{Nw7}**@CMO** sensor. However, for the ZnO_{Nw5}**@CMO** sensor, the maximum value of 85.5% is at an operating temperature of 150 °C. Future studies will focus on the optimization of sensors with the ZnO_{Nw}**@CMO** structure and on the testing at different concentrations of gasses.

Author Contributions: M.N. was involved in methodology, investigation, writing—original draft; C.B. was involved in methodology, investigation, writing—original draft; C.O. was involved in methodology, investigation, writing—original draft; V.P. was involved in writing and editing of the original draft; C.L. was involved in conceptualization, methodology, validation, investigation, writing—original draft, supervision; All authors have read and agreed to the published version of the manuscript.

Funding: This work was supported by a grant of the Ministry of Research, Innovation and Digitization, CNCS-UEFISCDI, project number PN-III-P1-1.1-TE-2021-0963, within PNCDI III, with contract number TE13/2022 (DD-CyT); by Project "Network of excellence in applied research and innovation for doctoral and postdoctoral programs/InoHubDoc", project co-funded by the European Social Fund financing agreement no. POCU/993/6/13/153437, and partially by project code PN 19 22 04 01 TINSME, 40 N/2019.

Institutional Review Board Statement: Not applicable.

Informed Consent Statement: Not applicable.

Data Availability Statement: Not applicable.

Acknowledgments: Authors would like to acknowledge the support provided by the Condensed Matter Department and to scientific researcher Maria Poienar, for delivering $CuMnO_2$ pristine.

Conflicts of Interest: The authors declare no conflict of interest. The funders had no role in the design of the study; in the collection, analyses, or interpretation of data; in the writing of the manuscript, or in the decision to publish the results.

References

1. Srinivasulu, K.; Shiv, G.S. Chemiresistive sensor based on zinc oxide nanoflakes for CO_2 detection. *ACS Appl. Nano Mater.* **2019**, *2*, 700–706. [CrossRef]
2. Zhang, C.; Xu, K.; Liu, K.; Xu, J.; Zheng, Z. Metal oxide resistive sensors for carbon dioxide detection. *Coord. Chem. Rev.* **2022**, *472*, 214758. [CrossRef]
3. Malcolm, A.; Wright, S.; Syms, R.R.; Dash, N.; Schwab, M.A.; Finlay, A. Miniature mass spectrometer systems based on a microengineered quadrupole filter. *Anal. Chem.* **2010**, *82*, 1751–1758. [CrossRef] [PubMed]
4. Severinghaus, J.W.; Bradley, A.F. Electrodes for blood pO_2 and pCO_2 determination. *J. Appl. Physiol.* **1958**, *13*, 515–520. [CrossRef] [PubMed]
5. Bültzingslowen, C.; McEvoy, A.K.; McDonagh, C.; MacCraith, B.D.; Klimant, I.; Krause, C.; Wolfbeis, O.S. Sol–gel based optical carbon dioxide sensor employing dual luminophore referencing for application in food packaging technology. *Analyst* **2002**, *127*, 1478–1483. [CrossRef] [PubMed]
6. Morio, M.; Hyodo, T.; Shimizu, Y.; Egashira, M. Effect of macrostructural control of an auxiliary layer on the CO_2 sensing properties of NASICON-based gas sensors. *Sens. Actuators B Chem.* **2009**, *139*, 563–569. [CrossRef]
7. Xu, S.; Li, C.; Li, H.; Li, M.; Qu, C.; Yang, B. Carbon dioxide sensors based on a surface acoustic wave device with a graphene-nickel-l-alanine multilayer film. *J. Mater. Chem.* **2015**, *C3*, 3882–3890. [CrossRef]
8. Tanvir, N.B.; Yurchenko, O.; Urban, G. Optimization study for work function-based CO_2 sensing using CuO-nanoparticles in respect to humidity and temperature. *Procedia Eng.* **2015**, *120*, 667–670. [CrossRef]
9. Herran, J.; Mandayo, G.G.; Castano, E. Physical behaviour of $BaTiO_3$–CuO thin film under carbon dioxide atmospheres. *Sens. Actuators B Chem.* **2007**, *127*, 370–375. [CrossRef]
10. Yueqiang, L.; Zhuangjun, F. Compositing strategies to enhance the performance of chemiresistive CO_2 gas sensors. *Mater. Sci. Semicond. Process.* **2020**, *107*, 104820–104841. [CrossRef]
11. Saruhan, B.; Fomekong, R.L.; Nahirniak, S. Review: Influences of Semiconductor Metal Oxide Properties on Gas Sensing Characteristics. *Front. Sens.* **2021**, *2*, 657931. [CrossRef]
12. Ren, H.; Weng, H.; Zhao, P.; Zuo, R.; Lu, X.; Huang, J. Preparation of porous sea-urchin-like CuO/ZnO composite nanostructure consisting of numerous nanowires with improved gas-sensing performance. *Front. Mater. Sci.* **2022**, *16*, 220583. [CrossRef]
13. Zhang, Y.; Ram, M.K.; Stefanakos, E.K.; Goswami, D.Y. Synthesis, characterization and applications of ZnO nanowires. *J. Nanomater.* **2012**, *2012*, 22. [CrossRef]
14. Wan, H.; Ruda, H.E. A study of the growth mechanism of CVD-grown ZnO nanowires. *J. Mater. Sci. Mater. Electron.* **2010**, *21*, 1014–1019. [CrossRef]
15. Wang, X.D.; Song, J.H.; Wang, Z.L. Nanowire and nanobelt arrays of zinc oxide from synthesis to properties and to novel devices. *J. Mater. Chem.* **2007**, *17*, 711–720. [CrossRef]
16. Chu, D.; Masuda, Y.; Ohji, T.; Kato, K. Formation and photocatalytic application of ZnO nanotubes using aqueous solution. *Langmuir* **2009**, *26*, 2811–2815. [CrossRef]
17. Yu, H.; Zhang, Z.; Han, M.; Hao, X.; Zhu, F. A general low-temperature route for large-scale fabrication of highly oriented ZnO nanorod/nanotube arrays. *J. Am. Chem. Soc.* **2005**, *127*, 2378–2379. [CrossRef]
18. Ding, Y.; Kong, X.Y.; Wang, Z.L. Doping and planar defects in the formation of single-crystal ZnO nanorings. *Phys. Rev. B* **2004**, *70*, 235408. [CrossRef]
19. Tneh, S.S.; Abu Hassan, H.; Saw, K.G.; Yam, F.K.; Hassan, Z. Structural and optical properties of large-scale ZnO nanowires and nanosheets prepared by dry thermal oxidation. *Surf. Rev. Lett.* **2009**, *16*, 901–904. [CrossRef]
20. Li, J.; Peng, H.; Liu, J.; Everitt, H.O. Facile gram-scale growth of single-crystalline nanotetrapod-assembled ZnO through a rapid process. *Eur. J. Inorg. Chem.* **2008**, *20*, 3172–3176. [CrossRef]
21. Park, W.I.; Yi, G.C.; Kim, M.; Pennycook, S.J. ZnO nanoneedles grown vertically on Si substrates by non-catalytic vapor-phase Epitaxy. *Adv. Mater.* **2002**, *14*, 1841–1843. [CrossRef]
22. Dai, Z.R.; Pan, Z.W.; Wang, Z.L. Novel nanostructures of functional oxides synthesized by thermal evaporation. *Adv. Funct. Mater.* **2003**, *13*, 9–24. [CrossRef]
23. Duan, X.F.; Lieber, C.M. Laser-assisted catalytic growth of single crystal GaN nanowires. *J. Am. Chem. Soc.* **2000**, *112*, 188–189. [CrossRef]
24. Li, Y.; Meng, G.W.; Zhang, L.D. Ordered semiconductor ZnO nanowire arrays and their photoluminescence properties. *Appl. Phys. Lett.* **2000**, *76*, 126238. [CrossRef]
25. Ren, S.; Bai, Y.F.; Chen, J.; Deng, S.Z.; Xu, N.S.; Wu, Q.B.; Yang, S.; Phillip, F. Catalyst-free synthesis of ZnO nanowire arrays on zinc substrate by low temperature thermal oxidation. *Mater. Lett.* **2007**, *61*, 666–670. [CrossRef]
26. Yuan, L.; Wang, C.; Cai, R.; Wang, Y.; Zhou, G. Temperature-dependent growth mechanism and microstructure of ZnO nanostructures grown from the thermal oxidation of zinc. *J. Cryst. Growth* **2014**, *390*, 101–108. [CrossRef]
27. Florica, C.; Preda, N.; Costas, A.; Zgura, I.; Enculescu, I. ZnO nanowires grown directly on zinc foils by thermal oxidation in air: Wetting and water adhesion properties. *Mat. Lett.* **2016**, *170*, 156–159. [CrossRef]
28. Galstyan, V.; Moumen, A.; Kumarage, G.W.C.; Comini, E. Progress towards chemical gas sensors: Nanowires and 2D semiconductors. *Sens. Actuators B Chem.* **2022**, *357*, 131466. [CrossRef]

29. Huang, B.; Zhang, Z.; Zhao, C.; Cairang, L.; Bai, J.; Zhang, Y.; Mu, X.; Du, J.; Wang, H.; Pan, X.; et al. Enhanced gas-sensing performance of ZnO@In_2O_3 core@ shell nanofibers prepared by coaxial electrospinning. *Sens. Actuators* **2018**, *255*, 2248–2257. [CrossRef]
30. Chang, C.-J.; Hung, S.-T.; Lin, C.-K.; Chen, C.-Y.; Kuo, E.-H. Selective growth of ZnO nanorods for gas sensors using ink-jet printing and hydrothermal processes. *Thin Solid Films* **2010**, *519*, 1693–1698. [CrossRef]
31. Chang, C.-J.; Lin, C.-Y.; Chen, J.-K.; Hsu, M.-H. Ce-doped ZnO nanorods based low operation temperature NO_2 gas sensors. *Ceram. Int.* **2014**, *40*, 10867–10875. [CrossRef]
32. Han, C.; Li, X.; Shao, C.; Li, X.; Ma, J.; Zhang, X.; Liu, Y. Composition-controllable p-CuO/n-ZnO hollow nanofibers for high-performance H_2S detection. *Sens. Actuators* **2019**, *285*, 495–503. [CrossRef]
33. Kang, Y.; Yu, F.; Zhang, L.; Wang, W.; Chen, L.; Li, Y. Review of ZnO-based nanomaterials in gas sensors. *Solid State Ion.* **2021**, *360*, 115544–115566. [CrossRef]
34. Keerthana, S.; Rathnakannan, K. Hierarchical ZnO/CuO nanostructures for room temperature detection of carbon dioxide. *J. Alloys Compd.* **2022**, *897*, 162988. [CrossRef]
35. Hsu, C.L.; Chang, E.C.; Hsueh, H.T.; Liu, Y.H. Solution-synthesized p-type $CuMnO_2$ and n-type ZnO to form the core-shell nanowires for photo and gas sensing. *J. Alloys Compd.* **2022**, *899*, 163380. [CrossRef]
36. Lazau, C.; Poienar, M.; Orha, C.; Ursu, D.; Nicolaescu, M.; Vajda, M.; Bandas, C. Development of a new "n-p" heterojunction based on TiO_2 and $CuMnO_2$ synergy materials. *Mater. Chem. Phys.* **2021**, *272*, 124999. [CrossRef]
37. Nicolaescu, M.; Bandas, C.; Orha, C.; Şerban, V.; Lazău, C.; Căprărescu, S. Fabrication of a UV photodetector based on n-TiO_2/p-$CuMnO_2$ heterostructures. *Coatings* **2021**, *11*, 1380. [CrossRef]
38. Lazau, C.; Nicolaescu, M.; Orha, C.; Şerban, V.; Bandas, C. Self-Powered Photodetector Based on FTO/n-TiO_2/p-$CuMnO_2$ Transparent Thin Films. *Materials* **2022**, *15*, 5229. [CrossRef]
39. Poienar, M.; Banica, R.; Sfirloaga, P.; Ianasi, C.; Mihali, C.V.; Vlazan, P. Microwave-assisted hydrothermal synthesis and catalytic activity study of crednerite-type $CuMnO_2$ materials. *Ceram. Int.* **2018**, *44*, 6157–6161. [CrossRef]
40. Lin, C.-F.; Chao, L.-C. ZnO nanowires prepared by thermal oxidation of metallic zinc films. In Proceedings of the 3rd International Nanoelectronics Confference (INEC), Hong Kong, China, 3–8 January 2010; pp. 1074–1075. [CrossRef]
41. Khanlary, M.R.; Vahedi, V.; Reyhani, A. Synthesis and characterization of ZnO nanowires by thermal oxidation of Zn thin films at various temperatures. *Molecules* **2012**, *17*, 5021–5029. [CrossRef]
42. Zhang, B.P.; Binh, N.T.; Segawa, Y.; Wakatsuki, K.; Usami, N. Optical properties of ZnO rods formed by metalorganic chemical vapor deposition. *Appl. Phys. Lett.* **2003**, *83*, 1635–1637. [CrossRef]
43. Yang, S.; Lei, G.; Xu, H.; Lan, Z.; Wang, Z.; Gu, H. Metal Oxide Based Heterojunctions for Gas Sensors: A Review. *Nanomaterials* **2021**, *11*, 1026. [CrossRef] [PubMed]
44. Brillson, L.J.; Lu, Y. ZnO Schottky barriers and Ohmic contacts. *J. Appl. Phys.* **2011**, *109*, 121301. [CrossRef]
45. Hossein-Babaei, F.; Lajvardi, M.M.; Alaei-Sheini, N. The energy barrier at noble metal/TiO_2 junctions. *Appl. Phys. Lett.* **2015**, *106*, 083503. [CrossRef]
46. Brötzmann, M.; Vetter, U.; Hofsäss, H. BN/ZnO heterojunction diodes with apparently giant ideality factors. *J. Appl. Phys.* **2009**, *106*, 063704. [CrossRef]
47. Harnack, O.; Pacholski, C.; Weller, H.; Yasuda, A.; Wessels, J.M. Rectifying Behavior of Electrically Aligned ZnO Nanorods. *Nano Lett.* **2003**, *3*, 1097–1101. [CrossRef]
48. Lao, C.S.; Liu., J.; Gao, P.; Zhang, L.; Davidovic, D.; Tummala, R.; Wang, Z.L. ZnO Nanobelt/Nanowire Schottky Diodes Formed by Dielectrophoresis Alignment across Au Electrodes. *Nano Lett.* **2006**, *6*, 263–266. [CrossRef]
49. Kumar, M.; Bhat, T.N.; Rajpalke, M.K.; Roul, B.; Kalghatgi, A.T.; Krupanidhi, S.B. Transport and infrared photoresponse properties of InN nanorods/Si heterojunction. *Nanoscale Res. Lett.* **2011**, *6*, 609. [CrossRef]
50. Um, H.-D.; Moiz, S.A.; Park, K.-T.; Jung, J.-Y.; Jee, S.-W.; Ahn, C.H.; Kim, D.C.; Cho, H.K.; Kim, D.-W.; Lee, J.-H. Highly selective spectral response with enhanced responsivity of n-ZnO/p-Si radial heterojunction nanowire photodiodes. *Appl. Phys. Lett.* **2011**, *98*, 033102. [CrossRef]
51. Breitenstein, O.; Altermatt, P.; Ramspeck, K.; Schenk, A. The Origin of ideality factors n > 2 of shunts and surfaces in the dark I-V curves of Si solar cells. In Proceedings of the 21st European Photovoltaic Solar Energy Conference, Dresden, Germany, 4–8 September 2006.
52. Hsu, K.-C.; Fang, T.-H.; Hsiao, Y.-J.; Wu, P.-C. Response and characteristics of TiO_2/perovskite heterojunctions for CO gas sensors. *J. Alloys Compd.* **2019**, *794*, 576–584. [CrossRef]
53. Amarnath, M.; Gurunathan, K. Highly selective CO_2 gas sensor using stabilized NiO-In_2O_3 nanospheres coated reduced graphene oxide sensing electrodes at room temperature. *J. Alloys Compd.* **2021**, *857*, 157584. [CrossRef]
54. González-Garnica, M.; Galdámez-Martínez, A.; Malagón, F.; Ramos, C.D.; Santana, G.; Abolhassani, R.; Kumar Panda, P.; Kaushik, A.; Mishra, Y.K.; Karthik, T.V.K.; et al. One dimensional Au-ZnO hybrid nanostructures based CO_2 detection: Growth mechanism and role of the seed layer on sensing performance. *Sens. Actuators B Chem.* **2021**, *337*, 129765. [CrossRef]

55. Jeong, Y.J.; Balamurugan, C.; Lee, D.W. Enhanced CO_2 gas-sensing performance of ZnO nanopowder by La loaded during simple hydrothermal method. *Sens. Actuators B Chem.* **2016**, *229*, 288–296. [CrossRef]
56. Kumar, A.; Sanger, A.; Kumar, A.; Chandra, R. Highly sensitive and selective CO gas sensor based on a hydrophobic SnO_2/CuO bilayer. *RSC Adv.* **2016**, *6*, 47178–47184. [CrossRef]
57. Hung, S.-T.; Chang, C.-J.; Hsu, C.-H.; Chu, B.H.; Lo, C.F.; Hsu, C.-C.; Pearton, S.J.; Holzworth, M.R.; Whiting, P.G.; Rudawski, N.G.; et al. SnO_2 functionalized AlGaN/GaN high electron mobility transistor for hydrogen sensing applications. *Int. J. Hydrog. Energy* **2012**, *37*, 13783–13788. [CrossRef]
58. Chen, Y.; Zhu, C.L.; Xiao, G. Reduced-temperature ethanol sensing characteristics of flower-like ZnO nanorods synthesized by a sonochemical method. *Nanotechnology* **2006**, *17*, 4537–4541. [CrossRef]